13th International Symposium on Particle Image Velocimetry – ISPIV 2019
Munich, Germany, July 22-24, 2019

High-speed tomographic PIV of cylinder wakes in a shock tube using a pulse-burst laser

Kyle P. Lynch[1]* and Justin L. Wagner[1]

[1]Sandia National Laboratories, Aerosciences Department, Albuquerque, NM, USA

*Corresponding author: klynch@sandia.gov

Abstract

High-speed tomographic particle image velocimetry measurements describing flow development in cylinder wakes at Reynolds numbers from 8,200 to 53,000 is presented. Experiments are conducted in a shock tube, which creates an impulsive start followed by uniform flow conditions for 8.0 ms. A pulse-burst laser is used for illumination, allowing a larger measurement volume compared to typical high-speed setups (approximately 10x larger) with traditional oil-droplet particle seeding in air. Measurements are acquired at 10 kHz, allowing 90 snapshots to be acquired per shot. Additional advances are made in the data processing: single-image self-calibration accounts for shock tube recoil and distributed cluster processing allows compilation of a large dataset for statistical analysis. The initial wake development and transition to regular von Kármán shedding in the cylinder wake is shown in terms of the vortex topology, and statistics of vorticity components and the recirculation region are shown as a function of time and Reynolds number. Analysis of multiple runs and conditions shows an initially rapid development of spanwise vorticity, with a slow development in streamwise/transverse vorticity that peaks at the time of the first shedding cycle and assumes periodic shedding afterwards.

1 Introduction

Impulsively-started flow around cylinders is a classic configuration in fluid dynamics and is relevant to industrial applications such as blast and gust loading. The startup transient can be marked using a non-dimensional timescale t^*, equal to tU_∞/D, where t is time, U_∞ is the steady velocity following the impulsive start, and D is the cylinder diameter. Immediately following the start at $t^* = 0$, the flow develops a pair of symmetric vortices which grow in time. As noted by (Sarpkaya, 1966), this period of symmetric vortex development is also associated with a temporary rise in drag compared to the fully established wake. The instability of this symmetric configuration causes one vortex to lead the other as seen in the visualizations (Nagata, et al., 1975), leading to asymmetric shedding; length scales and fluctuation amplitudes are initially below the steady-state asymmetric wake. This continues until about t* = 20, after which the wake exhibits steady-state properties (Wagner, et al., 2018).

Most impulsively-started wake studies have applied planar methods such as light sheet visualization (Sarpkaya, 1966; Nagata, et al., 1975), PIV (Wagner, et al., 2018), or line-of-sight integrated methods such as interferometry (Asher & Dosanjh, 1968), to study the development and breakdown of the starting vortices. There have been fewer measurements on the *spanwise* development. The existence of spanwise features in steady cylinder wakes is well-established (Williamson, 1996). Beginning at a Reynolds number of approximately 200, a waviness of the primary spanwise-oriented vortex is observed ranging from 0.25-0.35 wavenumbers (based on cylinder diameter) and is termed mode A. At Re > 230, a transition occurs to a shorter-wavelength instability of around 1 wavenumber, mode B. Additional large-scale features are vortex dislocations, caused by

phase variations in the primary vortex in the near wake. These rapidly grow, breaking the spanwise continuity of the primary vortex and becoming large lambda-shaped structures (Williamson, 1992). At Re greater than about 1400, the separated shear layers become turbulent, leading to small-scale, spanwise-oriented vortices (Williamson, 1996).

There is little, if any, data available on these features in high Reynolds number impulsive wakes. Several questions arise: What is the startup time for individual features? Does the flow exhibit characteristics of modes A and B for a transient period at higher Reynolds numbers? Is vortex dislocation prominent during the start? Is there a relationship between streamwise and spanwise vorticity? This work aims to answer these by investigating feature development using time-resolved tomographic PIV. The use of time-resolved tomographic PIV in the context of high-speed air flows incurs numerous challenges, which this paper first addresses before moving on to these questions.

Time-resolved tomographic PIV has emerged as a powerful technique for spatio-temporal measurements. Most large-volume experiments have been performed in water due to the long timescales of interest and suitability of large tracer particles. In air flows, aerosol particles typically are used which are smaller and have dramatically lower scattering performance. Further, the shorter timescales encountered in air flows require a higher pulse repetition rate which generally yields lower laser pulse energy. Three additional factors also constrain the volume thickness: first, a linearly proportional decrease in laser fluence occurs as the depth increases. second, maintaining depth-of-focus through a thick volume requires a reduction in camera aperture (higher f/#), reducing the collected light. third, the increased diffraction spot size at higher f/# spreads the particle image across a larger portion of the sensor resulting in lower particle image contrast.

Due to these signal constraints, high-speed measurements in air typically rely on multi-pass laser arrangements and/or multiple independent systems. The former creates an optical cavity encompassing the measurement volume (Ghaemi & Scarano, 2010), which multiplies the signal by a large factor (approx. 5-7) and is particularly useful for DPSS laser sources with low pulse energies (typically 5-20 mJ/pulse at 20 kHz). However, even using this arrangement, the reduction in pulse energy with increasing repetition rate for DPSS systems restricts this method to low-speed flows (typ. under 15 m/s) and thin volumes (typ. under 5 mm). For example, using such an arrangement (Ghaemi & Scarano, 2011) achieved a volume of 17.6 cm^3 at 2.7 kHz. However, at 10 kHz, (Probsting, et al., 2015) was constrained to only a 3.6 cm^3 volume. In contrast, multi-pulse systems use two double-pulse systems which can be configured to achieve arbitrary delays between pulse pairs (Lynch & Scarano, 2014; Schroder, et al., 2013). These systems are suitable for high-speed flows and thick volumes due to the high pulse energy of the independent lasers. Unfortunately, only four particle images are acquired, which limits their utility for quantifying the evolution of dynamic phenomena.

The signal level for a given imaging configuration can be increased by using more powerful illumination or particles with more favorable scattering performance. The latter has been demonstrated using helium-filled soap bubbles to enable very large measurement volumes for low-speed air flows (Scarano, et al., 2015); however, these tracers are not suitable for shock tubes or high-speed wind tunnels, which subject particles to significant pressure gradients. Therefore, the remaining alternative is to increase the laser energy. Most commercially-available DPSS lasers operate at a maximum repetition rate around 10-20 kHz, with pulse energy between 5-40 mJ/pulse. This is much less than the 100s of mJ/pulse available with standard dual-cavity Nd:YAG lasers.

An attractive alternative is a *pulse-burst* laser, which has an architecture enabling operation at the high repetition rate of DPSS sources, but with the high energy of standard flashlamp-pumped Nd:YAG sources. The recent commercialization of these previously custom-built research devices makes them suitable for industrial use. Investigations have used pulse-burst lasers for time-resolved planar PIV in aerodynamic test facilities (Wagner, et al., 2018; Vanstone, et al., 2016), but there are fewer examples of pulse-burst lasers applied for large-volume tomographic PIV. To the authors' knowledge, the only examples were concurrently presented by (Yi, et al., 2018) and (Lynch & Wagner, 2018). This work extends the latter and provides two contributions: first, to demonstrate the feasibility of using a pulse-burst laser to perform large-volume time-resolved tomographic PIV in high-speed air flows;

and second, to use the unique capability for quantitative measurements of three-dimensional vortex organization in an impulsively-started cylinder wake.

2 Experimental Arrangement

Experiments are performed in the Multiphase Shock Tube (MST) at Sandia National Laboratories, described in detail in (Wagner, et al., 2012). The MST consists of a circular driver section 8.9 cm in diameter and 2.1 m long, and a square driven section 7.9 cm height/width with a length of 6.4 m. The driver is pressurized with nitrogen at room temperature, and the driven is filled with air at room temperature and local atmospheric pressure of 84.1 kPa. In lieu of burst disks, a fast-acting valve is used (Dynamic Systems Research, model 725-3.0-6000).

A characterization of test section flow conditions was reported for high driver pressures (Wagner, et al., 2018); for the low pressures used in this study, a characterization is shown in figure 1, acquired using pulse-burst planar PIV along a centerline plane. . Repeatability is achieved in the initial startup transient and constant velocity interval. The 50-psi case shows an increase in the freestream velocity during the run, consistent with boundary layer growth effects in shock tubes (Mirels & Braun, 1957).

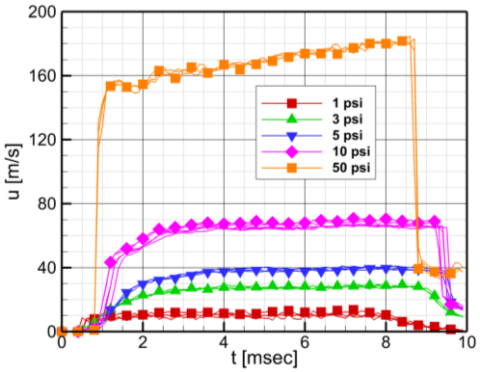

Figure 1: Freestream velocity for empty shock tube at the test section. Data from pulse-burst planar PIV along a centerline plane. Overlays at each condition correspond to three runs.

Driver Pres. [psig]	Induced Velocity [m/s]	Velocity [m/s]	Shock Mach [-]	Re_D [-]	t^*_{max} [-]	Δt_1 [µs]	$\Delta t_2 / \Delta t_1$ [-]
3.0	28.0	32.7	1.05	22,800	18.0	7.0	14.7
5.0	38.0	44.3	1.07	31,000	25.0	5.0	19.9
10.0	65.0	76.0	1.13	53,000	41.0	2.9	34.1
50.0	160	186	1.33	130,400	101	1.3	76.1

Table 1. Flow and timing conditions.

The test model is a circular cross-section cylinder of diameter 1.40 cm and length 7.62 cm. It is rigidly bolted to the acrylic floor and ceiling of the test section at a location 4.4 m downstream from the valve. The model spans the test section with no accommodations at the sidewall juncture. Matte black primer was applied to reduce laser reflections. The cameras viewed through an AR-coated fused silica window (17.8 cm width, 6.4 cm height, 3.2 cm thickness) acting as a test section sidewall.

Illumination is provided by a pulse-burst laser (Quasi-Modo by Spectral Energies, LLC). This incorporates a master-oscillator/power-amplifier (MOPA) architecture with a fiber-coupled pre-amplifier, high-gain diode-pumped amplifiers, and flashlamp-pumped power amplifiers (Slipchenko, et al., 2012; Slipchenko, et al., 2013). The laser can generate a burst of pulses at rates of 5 kHz to 500 kHz with pulse energies at 532 nm of 500 mJ and 20 mJ, respectively. To produce such large energies at high repetition rates, the laser has a low duty cycle: it can fire once every Δt_{burst} of 8 seconds with a maximum burst duration T_{burst} of 10.5 ms. The burst duration is longer than the typical test time in the shock tube, making it an ideal tool for measurements in a transient facility. For PIV, the laser is operated in a doublet mode where the inter-pulse time Δt_1 and the inter-pair time Δt_2 can be independently adjusted as illustrated in figure 2. The Δt_1 is set for maximum particle displacement of approximately 10 voxels and is varied from 1.3 µs to10 µs according to the flow conditions. The Δt_2 is set based on the cameras' maximum frame rate at full resolution (20 kHz, see below), operating in a

'frame-straddling' configuration shown in figure 2 with exposure time t_{exp}. This fixes Δt_2 to 100 µs (10 kHz) for all cases.

At 10 kHz the laser produces 380 mJ/pulse (760 mJ/pulse pair). The beam is shaped into a volume 44 x 44 x 15/19 mm, aligned as in figure 3. The 15 mm case (measurement volume 1) focuses on the shear layer development on one side of the cylinder. The 19 mm case (measurement volume 2) focuses on the separation region and is centered on the cylinder axis. These volumes of 29/37 cm^3 with aspect ratios of 3.5/2.3 are roughly a factor of 10 larger than previous tomographic volumes conducted at a rate exceeding a few kHz in air with standard aerosol seeding. For this paper, only data from measurement volume 1 is considered.

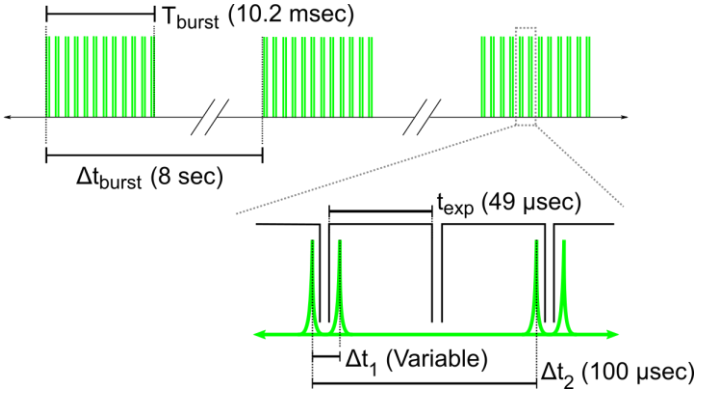

Figure 2: Timing diagram for pulse-burst operation in doublet mode employing frame-straddling.

Seeding is produced by an atomizer (TSI 9306), yielding di-ethyl-hexyl-sebecate (DEHS) droplets of nominally 1.6 µm diameter. These are introduced through a valve 3.0 m upstream of the test section. A second valve is located at the end of the shock tube and connected to an exhaust fume hood. The seeding inlet pressure is varied to achieve a low flow of uniform seeding density before the run.

Four Photron SA-Zs (1024 x 1024 pixels at 20 kHz, 20 µm pixel size) are used in a linear configuration with a total angular aperture of 50 deg. Each camera is equipped with 105 mm focal length lenses set to f/#=22 and mounted to Schiempflug adapters. Diffusion/peak-locking reduction filters were used to increase the particle image diameter from approximately 1.4 px to 1.8 px to aid reconstruction (Michaelis, et al., 2016). The physical scaling based on the sensor size is 24.7 px/mm. Note that the volume thickness slightly exceeds the depth of field due to the high magnification and will result in blurring of the particles near the edges of the reconstructed volume.

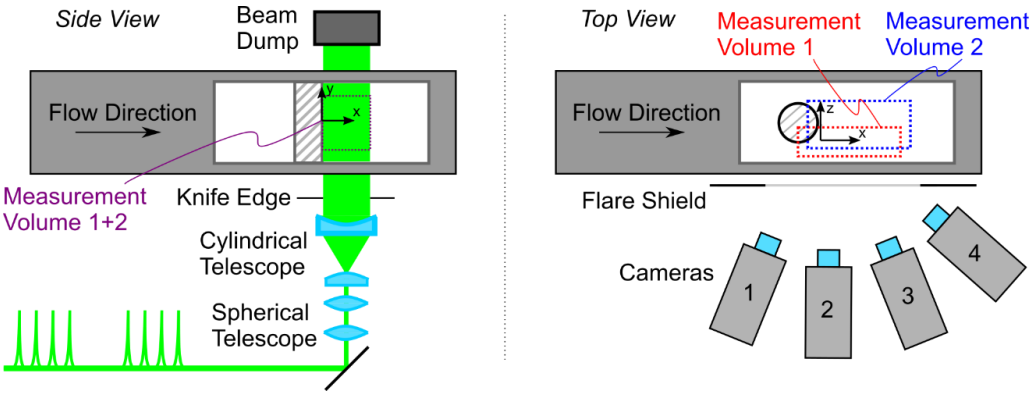

Figure 3. Diagram of laser, camera, and test section configuration. Schematic not to scale. Two measurement volumes view different transverse extents of the cylinder.

3 Data Analysis

Processing consisted of physical calibration, volume self-calibration (VSC), reconstruction, and cross-correlation. Physical calibration was performed using a single image of a LaVision 058-15 (5 mm dot spacing) dual-plane plate aligned to the top of the cylinder at indicated in figure 3 as z = 0 mm. A third-order polynomial fit on 60 points per plane yielded a calibration error of 0.2 px for all cameras. The calibration was extended to the full volume depth using the VSC (Wieneke, 2008).

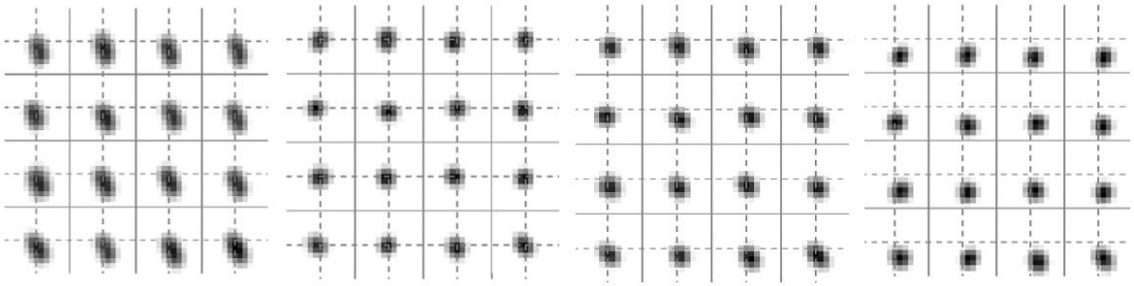

Figure 4. Variation in VSC disparity maps during a run for camera 2 at z = 0 mm.

VSC was applied to subsets of each run, revealing a repeatable, time-dependent drift beginning around 2 ms as shown by the disparity maps in figure 4. In (a), the full sequence is used to calculate the disparity map; subsets are shown in (b-d). The subsets show narrow disparity peaks that shift over time. The shift was over 1.5 px, enough to cause particle reconstruction to fail. This drift is caused by motion of the shock tube itself during a run, which transmits an impulsive force through the support structure to the cameras.

A software-based fix was implemented based on a single-image vibration-correction scheme (Michaelis & Wolf, 2011). VSC is performed for each image pair prior to reconstruction using a small search radius and small number of clustering bins to maintain sufficient signal. This reduced the disparity to under 0.1 pixels throughout the sequence as shown in figure 5. The requirement for calibration accuracy has been shown to be under 0.5 px for a reconstruction of sufficient quality, i.e., normalized cross-correlation coefficient to reference volume Q > 0.75, for particle image diameters of 3.0 px (Elsinga, et al., 2006); the sensitivity is expected to be greater in the current experiment due to the smaller particle image diameter of 1.8 px.

The effect of the calibration disparity is evident in the reconstruction signal-to-noise ratio shown in figure 6. As illustrated in the figure, this is defined as the ratio of the average intensity within the laser sheet to the regions outside the laser sheet; a value of 2.0 is considered a lower bound for a successful reconstruction (Scarano, 2013). The initial SNR is approximately 4 but declines and reaches a plateau of around 3. Without single-image self-calibration, the SNR reduces to a value of 1, indicating an unsuccessful reconstruction. This reduction begins at approximately 2 msec, which is consistent for both frames with the disparity magnitude exceeding approximately 0.25 pixels per figure 5. Note, the oscillatory behavior of the SNR is due to small variations in seeding density within the recirculation bubble during the shedding cycle.

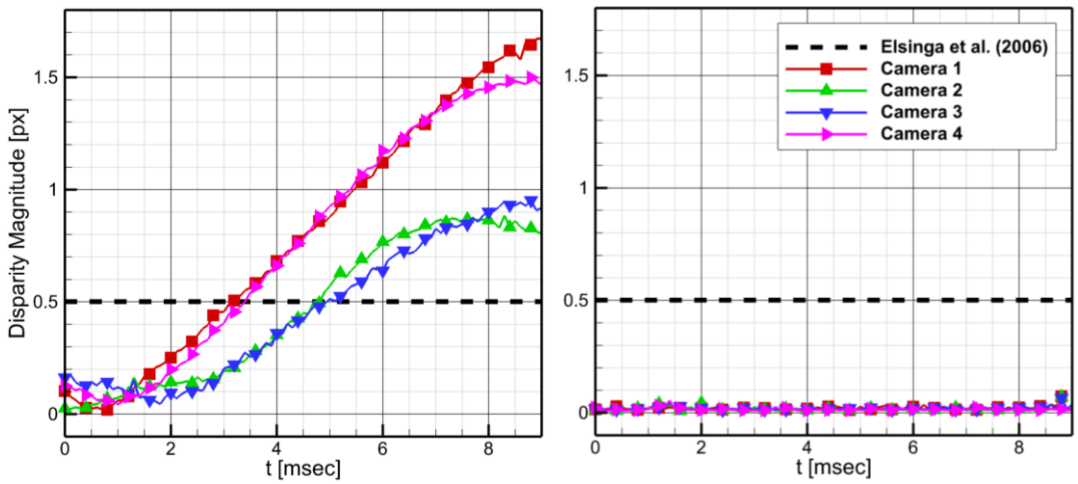

Figure 5. Average VSC disparity magnitude for each camera for a single run without (left) and with (right) vibration correction scheme based on single-image self-calibration.

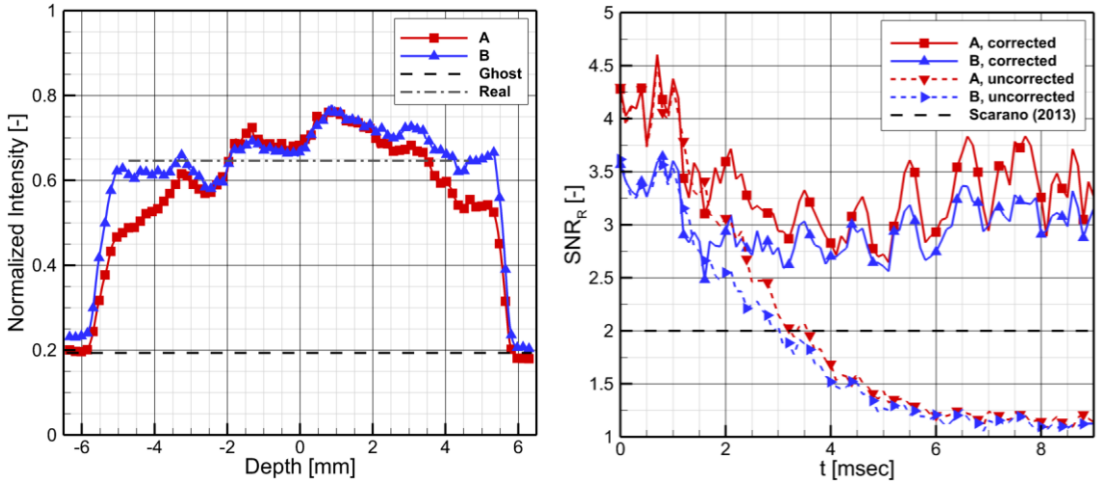

Figure 6. Left, Average reconstructed z-intensity profile for frames A and B with single-image self-calibration applied. Dashed lines indicate example intensities for calculation of the SNR. Right, SNR throughout the sequence with and without the single-image self-calibration. Data from run 1693, a 10 psi run.

Multiple options were considered for reconstruction and cross-correlation, aiming to operate at high particle density for maximizing spatial resolution despite the limited image resolution of high-speed cameras. The large ratio between Δt_2 and Δt_1 (see Table 1) excludes sequential reconstruction methods such as SMTE (Lynch & Scarano, 2015) and dense particle tracking methods such as STB (Schanz, et al., 2016). Therefore, the MTE approach is used (Novara, et al., 2010), modified to include a time-marching velocity predictor. A mask in the cross-correlation procedure reduces bias and outliers near the cylinder interface. Prior to these steps, image preprocessing consisted of a 31 x 31 px sliding minimum subtraction and a 100 x 100 px sliding average intensity normalization.

MTE has a high computational cost: for the current study 150 runs of 100 image pairs each were acquired to span the various conditions. Each run takes approximately 12 hours to process on a workstation. This suggests a total processing time of over two months. To avoid this, dataset-level parallelization distributed each run to a node of a computer cluster (Sandia 'Skybridge': 1850 nodes, 2 x Xeon E5-2670/node, 64 GB memory/node). This allowed the entire dataset to be processed in 11 hours, potentially a highly scalable alternative to GPU acceleration.

4 Flow Analysis

In figure 7, normalized vorticity contours give a visual overview of the flow development for a 38 m/s case (5 psi driver, Re_D = 31,000). In (a) the onset of vortical structure begins with the formation of a single spanwise-coherent vortex around 1.8 msec (t* = 5.4) after the shock passage and grows until about 2.0 msec (t* = 7.0). A transition begins, shown in (b-c), where the spanwise coherence of the initial vortex is broken by intermittent features, possibly corresponding to vortex dislocations as shown by the arrow. In (d), a reorientation occurs where the shed spanwise vortices begin aligning along the streamwise direction. The reorientation is complete by about t* = 20 in (e-f), where both spanwise and streamwise vortex features exist in the near and far wake, respectively. In comparison to initial times, the spanwise vortices notably are of smaller scale and frequency, with two to three vortices occurring over the recirculation region as indicated by the arrows. Not visible in the visualization is the organization of the streamwise vortices into counterrotating pairs.

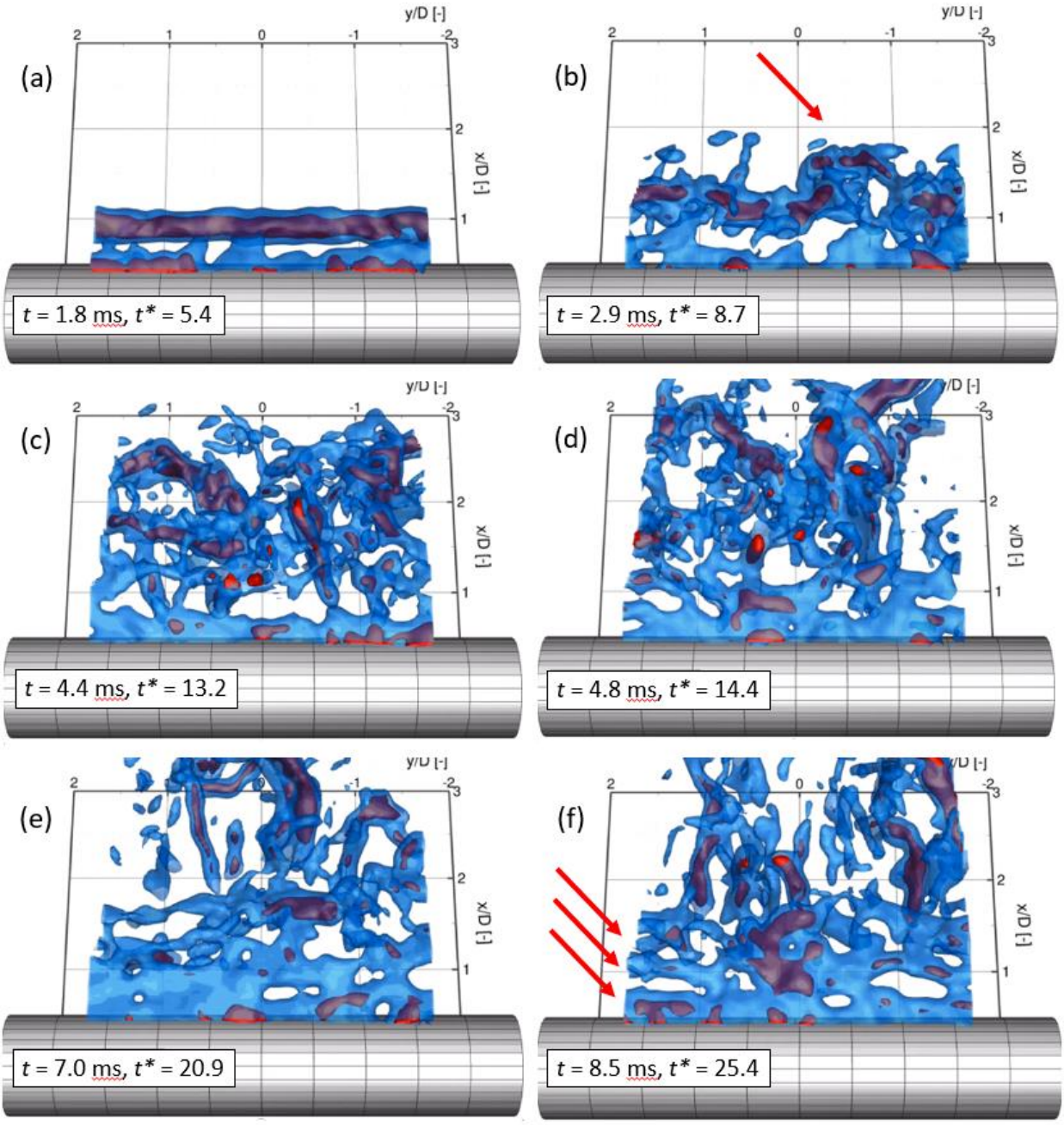

Figure 7. Vortex organization for Re_D = 31,000. Isosurfaces of normalized vorticity magnitude $\omega^* = \omega D/u_\infty$, values 6 (blue) and 10 (red).

An overview of bulk flow statistics is shown in figure 8 to illustrate the temporal evolution of the different flow conditions. Statistics of the vorticity field and the recirculation bubble size are included. The magnitude of the vorticity vector and each of its components is ensemble averaged over the entire volume; i.e., each data point represents the ensemble average value of an entire volumetric snapshot. The vorticity vector is initially aligned entirely along the span (ω_y). A growth of streamwise (ω_x) and transverse (ω_z) vorticity occurs until t* = 15 for Re=22,800 and 31,000, and t* = 18 for Re=53,000. To our knowledge, quantitative data on this time separation is not reported in the literature. The use of time-resolved 3D measurement to elucidate this observation is critical. However, At the highest Re=130,400, the lag between span and stream/transverse vorticity formation is not as clearly noticeable, perhaps due to the limited early time resolution.

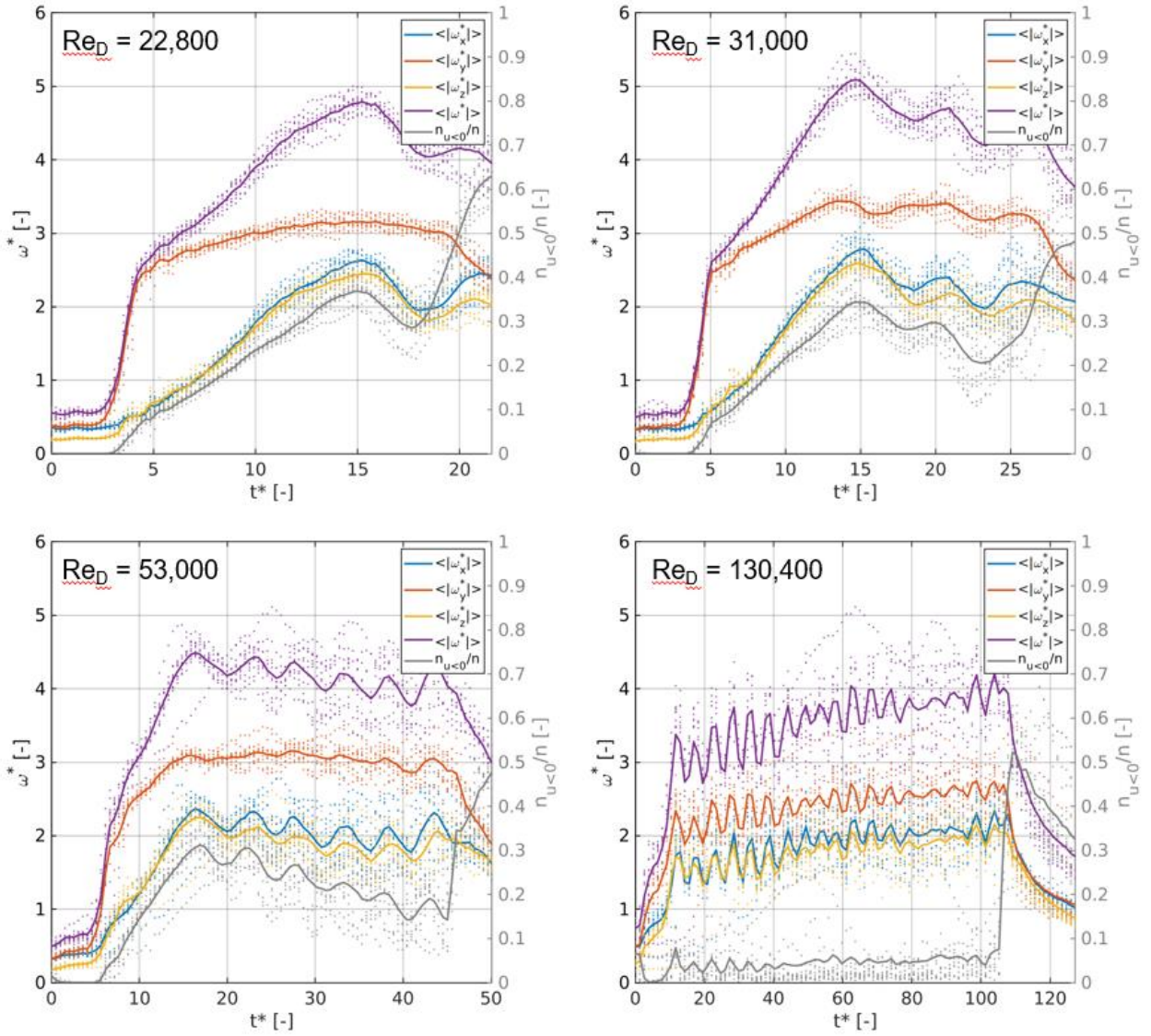

Figure 8. Vorticity distribution and recirculation bubble extent. Points represent ensemble average of all vectors in an individual snapshot, lines are averages of ensemble averages at each time.

Also, at this time of peak streamwise vorticity, the global maximum of the separation bubble size occurs (the increase in apparent separation bubble size near the end of the run signifies the end of the test with the reflected shock). Following this peak event, periodic shedding begins, characterized by streamwise/transverse vorticity alternating in intensity. The separation bubble extent also tracks this trend, growing to maximum size during times of peak streamwise/transverse vorticity. Interestingly, for the highest Re case, strong periodic behavior in the spanwise vorticity is observed, compared to a relatively constant value for lower Re.

The rapid rise of spanwise vorticity and delay in streamwise vorticity is due to the 'stationary' growth of the primary vortex until t* = 15-18. Evidence of this is shown in the time snapshots given in figure 9. The contour for each t* is an ensemble average of the runs at each flow condition, which are additionally span-averaged. Beginning at around t* = 4, the initial starting vortex grows in isolation near the cylinder. At around t* of 6, the vortex is spatially separated from the shear layer, and reaches its maximum extent before the influence of the symmetric vortex on the lower side of the cylinder constrains its growth. This Is clearly visible from t* of 8-10, where the vortical region is distorted in the streamwise direction as its growth is hampered in the transverse direction. Finally,

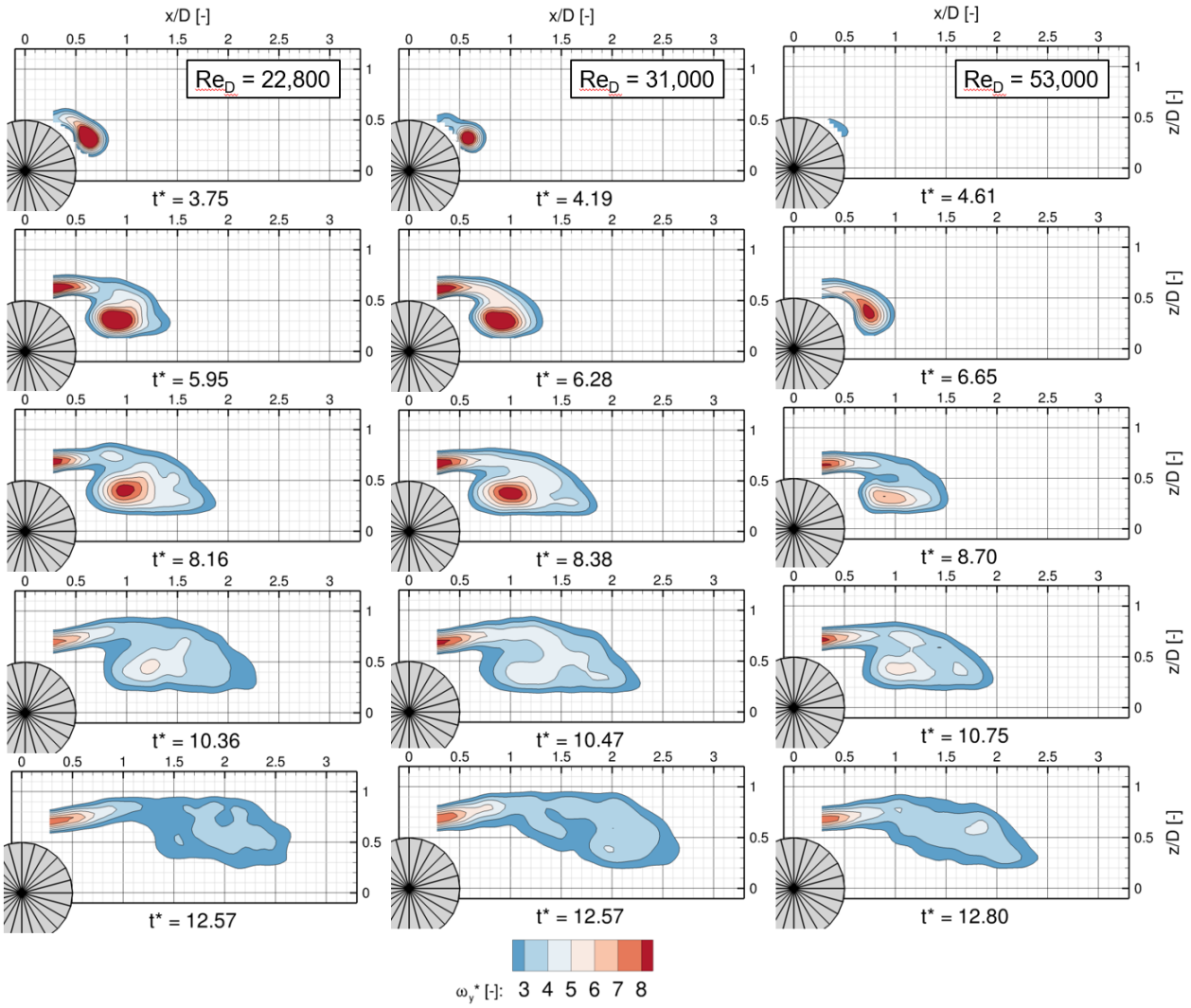

Figure 9. Spanwise vorticity distributions at ReD = 22,800 (left), 31,000 (center), and 53,000 (right). Data is ensemble averaged over all runs and across the cylinder span. Contours of spanwise vorticity.

at around t* = 12-13, the region has reached its maximum size and begins shedding, as observed by a large-scale motion of the vortical region downstream.

5 Conclusion

The main goals of this study were to demonstrate use of a pulse-burst laser to enable thick-volume time-resolved tomographic PIV in high-speed air flows and to use the capability for quantitative measurements of three-dimensional vortex organization in an impulsively-started cylinder wake. The pulse-burst laser enabled a successful measurement exceeding the speeds and volume sizes typical when using diode-pumped solid-state lasers. The primary challenge was facility vibration, which caused a relative camera motion beyond an acceptable calibration accuracy. Single-image self-calibration effectively nullified the calibration error. The success of the hardware arrangement and in-situ calibration correction enables a time-resolved 3-D velocimetry measurement capability in an industrial high-speed aerodynamics setting.

Analysis of the impulsively-started cylinder wake shows multiple phases: the initial startup is characterized by the formation of a large spanwise-coherent vortex beginning around t* = 4-5. This spanwise vortex grows while streamwise- and transverse-oriented vorticity develops from t* = 5-18.

It is observed in visualizations around this time that the spanwise vortex appears to reorient in the streamwise direction, perhaps due to large-scale vortex dislocations. Statistics of the large data set revealed a marked difference in the rise times between vorticity components, such that the spanwise component rapidly rises to a peak value, with a slow growth in streamwise and transverse vorticity. This behavior appears to be consistent across a range of Reynolds numbers. Also, during this time the extent of the separation bubble also increases. Regular shedding develops after this initial peak in streamwise/transverse vorticity.

Acknowledgements

The authors thank Seth Spitzer, Russell Spillers, Tom Grasser, and Paul Farias for assistance in the experimental setup. This work was supported by the Laboratory Directed Research and Development program at Sandia National Laboratories. The views expressed in the article do not necessarily represent the views of the U.S. Department of Energy or the United States Government. Sandia National Laboratories is a multi-mission laboratory managed and operated by National Technology and Engineering Solutions of Sandia, L.L.C., a wholly owned subsidiary of Honeywell International, Inc. for the U.S. Department of Energy's National Nuclear Security Administration under contract DE-NA0003525.

References

Asher, J. A. & Dosanjh, D. S., 1968. An experimental investigation of the formation and flow characteristics of an impulsively generated vortex street. Journal of Basic Engineering, Volume 90, pp. 596-606.

Elsinga, G. E., Scarano, F., Wieneke, B. & van Oudheusden, B. W., 2006. Tomographic particle image velocimetry. Experiments in Fluids, Volume 41, pp. 933-947.

Ghaemi, S. & Scarano, F., 2010. Multi-pass light amplification for tomographic particle image velocimetry. Measurement Science and Technology, Volume 21.

Ghaemi, S. & Scarano, F., 2011. Counter-hairpin vortices in the turbulent wake of a sharp trailing edge. Journal of Fluid Mechanics, Volume 689, pp. 317-356.

Lynch, K. P. & Scarano, F., 2014. Material acceleration estimation by four-pulse tomo-PIV. Measurement Science and Technology, Volume 25.

Lynch, K. P. & Scarano, F., 2015. An efficient and accurate approach to MTE-MART for time-resolved tomographic PIV. Experiments in Fluids, Volume 56.

Lynch, K. P. & Wagner, J. L., 2018. Time-resolved pulse-burst tomographic PIV of impulsively-started cylinder wakes in a shock tube. AIAA Paper 2018-2038.

Michaelis, D., Neal, D. R. & Wieneke, B., 2016. Peak-locking reduction for particle image velocimetry. Measurement Science and Technology, Volume 27.

Michaelis, D. & Wolf, C. C., 2011. Vibration compensation for tomographic PIV using single-volume self-calibration. PIV11.

Mirels, H. & Braun, W., 1957. Nonuniformities in shock-tube flow due to unsteady boundary layer action. TN-4021 NTN.

Nagata, H., Kakehi, Y., Tsunekawa, M. & Hasegawa, T., 1975. Unsteady flow past a circular cylinder started impulsively. Bulletin of the JSME.

Novara, M., Batenburg, K. J. & Scarano, F., 2010. Motion tracking-enhanced MART for tomographic PIV. Measurement Science and Technology, Volume 21.

Probsting, S., Tuinstra, M. & Scarano, F., 2015. Trailing edge noise estimation by tomographic particle image velocimetry. Journal of Sound and Vibration, Volume 346, pp. 117-138.

Sarpkaya, T., 1966. Separated flow about lifting bodies and impulsive flow about cylinders. AIAA Journal.

Scarano, F., 2013. Tomographic PIV: principles and practice. Measurement Science and Technology, Volume 24.

Scarano, F. et al., 2015. On the use of helium-filled soap bubbles for large-scale tomographic PIV in wind tunnel experiments. Exp Fluids, Volume 56.

Schanz, D., Gesemann, S. & Schroder, A., 2016. Shake-The-Box: Lagrangian particle tracking at high particle image densities. Experiments in Fluids, Volume 57.

Schroder, A. et al., 2013. Dual-volume and four-pulse tomo-PIV using polarized light.

Slipchenko, M. N. et al., 2012. Quasi-continuous burst-mode laser for high-speed planar imaging. Optics Letters, pp. 1346-1348.

Slipchenko, M. N. et al., 2013. All-diode-pumped quasi-continuous burst-mode laser for extended high-speed planar imaging. Optics Express, pp. 681-689.

Vanstone, L. et al., 2016. Investigation of unsteadiness in a Mach 2 swept-ramp shock/boundary-layer interaction using 50 kHz PIV. AIAA Paper 2016-3338.

Wagner, J. L. et al., 2012. A multiphase shock tube for shock wave interactions with dense particle fields. Experiments in Fluids, pp. 1507-1517.

Wagner, J. L. et al., 2018. Pulse-burst PIV of an impulsively started cylinder in a shock tube for Re > 105. Experiments in Fluids.

Wieneke, B., 2008. Volume self-calibration for 3D particle image velocimetry. Experiments in Fluids, Volume 45, pp. 549-556.

Williamson, C., 1992. The natural and forced formation of spot-like vortex dislocations in the transition of a wake. Journal of Fluid Mechanics, Volume 243.

Williamson, C., 1996. Vortex dynamics in the cylinder wake. Annual Review of Fluid Mechanics, Volume 28, pp. 477-539.

Yi, T. et al., 2018. Velocity gradient tensor upstream of the flame front with high-speed tomo-PIV/dual-plane-PIV/OH-PLIF measurements. AIAA Paper 2018-0153.